β-Grain Refinement in WAAM Ti-6Al-4V Processed with Inter-pass Ultrasonic Impact Peening

Vivek K. Sahu[1,3*], R. Biswal[2,4], A. E. Davis[1], X Chen[2], S.W. Williams[2], P.B. Prangnell[1]

[1]Department of Materials, The University of Manchester, Manchester, M13 9PL, UK

[2]Welding and Additive Manufacturing Centre, Cranfield University, Bedfordshire, United Kingdom, MK43 0PL

[3]Now at Mechanical Engineering, University of North Texas, Discovery Park, Denton, Texas, 76201, USA

[4]Now at Mechanical and Aerospace Systems Research Group, University of Nottingham, NG7 2TU

*Corresponding author: vivek.sahu@manchester.ac.uk, vivek.sahu@unt.edu

Abstract

As-deposited Wire-Arc Additive Manufactured (WAAM) Ti-6Al-4V parts typically contain large columnar β-grains on a centimetre scale, with a strong <001> fibre texture, leading to anisotropic mechanical properties and unacceptable scatter in damage tolerance. Inter-pass deformation, introduced by the application of Ultrasonic Impact Peening (UIP) across each added layer, has been shown to be effective in refining the β-grain structure and achieving a weaker texture. The depth of deformation and the grain refinement mechanism induced by UIP have been investigated by combining advanced electron backscatter diffraction (EBSD) characterization with a 'stop action' observation technique. UIP facilitates a similar refinement mechanism and nearly the same depth of deformation as conventional machine hammer peening, with the advantages of a much higher strain rate, lower peak force, and two orders of magnitude lower impact energy, making it a faster and more economical process. β recrystallization is seen within the deformation zone during re-heating through the $\alpha \rightarrow \beta$ transition. Although new recrystallized β grains formed in the UIP surface-deformed layer to a shallower depth than that of remelting, recrystallization initiated ahead of the melt pool and the recrystallized grains grew downwards to a greater depth before remelting. These refined grains were thus able to survive and act as nucleation sites at the fusion boundary for epitaxial regrowth during solidification, greatly refining the grain structure.

Keywords: ultrasonic impact peening; wire-arc additive manufacturing; titanium alloys; beta grain refinement; large area EBSD

1.0 Introduction

Directed energy deposition-wire arc additive manufacturing (DED-WAAM) with widely used titanium alloys like Ti-6Al-4V (Ti64) has recently attracted significant attention due to its capability for achieving high (4-10 kg hr^{-1}) deposition rates [1–4]. This advantage makes it a particularly promising technology for larger scale aerospace applications, owing to its capacity to produce meter-length near-net shape parts, with greater design flexibility and shorter lead times than conventional forgings [1,5]. However, without intervention as-built microstructures in WAAM Ti64 parts typically consist of coarse-columnar primary β grains with a strong solidification <001> fibre texture [6–10]. The development of such coarse columnar grain structures is attributed to epitaxial growth from the fusion boundary that continues uninterrupted through multiple deposition layers. This phenomenon occurs due to the close-to-unity partition coefficients of Al (k = 1.15) and V (k= 0.97) in Ti, coupled with a steep positive liquid thermal gradient at the solidification front in moving melt pool solidification [11–14]. The consequent low constitutional under cooling and narrow mushy zone, when combined with the lack of grain refiners in Ti alloys, effectively prevents new grain nucleation ahead of the solidification front [15].

In a WAAM deposition pass, a significant portion of the previous layer is remelted, depending on the processing conditions [16]. In addition, there is a substantial heat-affected zone (HAZ) below the energy source which results in the previously deposited 3-4 layers being reheated above the β-transus temperature (T$_β$), transforming fully back to β grains, before re-transforming during subsequent cooling to a multi-variant lamellar α microstructure, with a small amount of retained β [17]. Below this fully β-transformed region, HAZ bands are seen in the microstructure which are generated by coarsening of the α lamellae due to cyclic re-heating to temperatures high in the β-transus approach curve (in the range of 850 to ~ 1000 °C) [16].

Transformation to α on cooling after solidification leads to dilution of the texture seen in the β phase, due to the 12 variants possible from the Burgers Orientation relationship (BOR)[18]. However, the very strong primary β texture still influences the α texture sufficiently to result in mechanical anisotropy in as-built parts [18–23]. Moreover, the plastic heterogeneity caused by the nucleation of α on the coarse-aligned β-columnar grain boundaries and the α microtexture associated with different variants formed in each β grain leads to a lower strain to failure and greater uncertainty in other failure processes, such as fatigue crack growth rates [22]. Thus, it is important to explore the potential of techniques that can achieve a less textured, more refined, β-grain structure with the WAAM process and thereby more isotropic and consistent mechanical properties.

Many approaches have been investigated to refine the coarse β-grain structure normally found in WAAM Ti64 deposits and reduce their texture strength. These include; changing the solidification mode by increasing the wire feed speed[24], or modifying other deposition parameters [7,25,26], adding growth restrictors or inoculants [27–33], or applying inter-pass deformation by rolling [34–36] or peening [37–40]. All of these processes have advantages and disadvantages. For example, increasing the wire feed speed increases the deviation of the build surface profile, addition of elements like B and Y introduces brittle second phases [29,41]; and inter-pass deformation requires additional equipment and reduces the build rate [35,38].

When rolling deposited layers after solidification it has been shown that relatively low levels of plastic deformation (<12%) can result in high levels of β-grain refinement as well as substantial texture weakening [34,35]. The refinement mechanism has been attributed to recrystallization occurring during the α → β transformation. New β-grain orientations have also been suggested to form by annealing twinning as the migrating α-β interfaces encounter dislocations, causing growth faults, during rapid re-heating of the lightly deformed α lamellar microstructure [34,36].

Of the above approaches, inter-pass deformation by mechanical peening is worthy of more investigation as it is relatively simple to apply and does not involve modifications to the alloy chemistry, or a loss of the near-net-shape efficiency. In addition, peening also has the benefit of combating the build-up of residual stresses during deposition [42]. The repetitive impact action with a peening tool can be achieved either through a pneumatic[43], electromagnetic[44] or ultrasonic excitation mechanism [40,45]. Published results [37] have confirmed that grain refinement is controlled by the number of impacts per unit length times the energy delivered per impact, which has been referred to as line energy. In other words, the same line energy can be applied to a material using a low impact energy tool by increasing the number of impacts as with a high impact energy tool with a reduced number of impacts. With UIP, the travel speed, frequency, impact area, number of pins, and arrangement of pins will control the impact energy per unit length (line energy) applied to the workpiece. However, previous research on the effectiveness of peening has focused only on pneumatically excited Machine Hammer Peening (MHP) [37,38,42] where each impact was 6 J and the resultant line energy at a 10 mm/s travel speed was 12 J mm^{-1} [37]. 'Stop-action' experiments with MHP, where deposition was frozen midway to understand the interaction between energy source and deformed region ahead of the melt pool, have revealed that the depth of deformation required to produce new β-grain orientations on re-heating was only 0.5 mm below the surface, which was less than the re-melt depth (~ 0.7mm). However, new β-grain orientations were seen to develop within this thin peened surface layer ahead of the advancing energy source, which then grew downwards further below the peened surface as the energy source advanced. This allowed the new refined grains

to penetrate deeper than the melt pool depth and survive re-melting, to become the fusion boundary, where they then were able to reduce the grain size during solidification at the rear of the melt pool.

In comparison to a pneumatic MHP, to date no detailed study has been published on ultrasonic impact peening (UIP), which is the focus of the present work. While at first sight UIP is a closely related process, it operates at lower peak force (~1.5 kN) with 8 pins with better adoption of work piece surface curvature and the impact energy for each pin is estimated to be 20-70 mJ, whereas for pneumatic MHP the peak force per impact is higher (~4 kN) with energy imparted in each strike being two orders of magnitude higher (6 J). Both tools propagate energy into the deposited material by compression waves generated through high strain-rate impacts, with UIP applying higher velocity multi-pin impacts with a smaller peak force and pneumatic MHP applying relatively lower velocity, single pinned impact of higher peak force. In principle this gives UIP certain advantages over single pinned pneumatic MHP as UIP processing will be significantly faster, as well as the sound of impact being about 10 decibels lower due to smaller pin mass. The compression waves can propagate deep into the material, but will refract more off microstructure features where there is an abrupt change in elastic properties, like grain boundaries, as well as reflecting off the workpiece surfaces [40,45]. However, UIP cannot be assumed to behave the same as the single pinned and high energy pneumatic MHP and little is currently known about its effectiveness for β-grain refinement and the associated mechanisms involved. Therefore, the present work focuses on refinement mechanism by exploiting large area EBSD and EBSD-LAM technique to assess the depth of plastic deformation from the top surface, as well as the 'stop action' sample freezing of the melt pool to observe the microstructure evolution ahead of the melt pool after UIP.
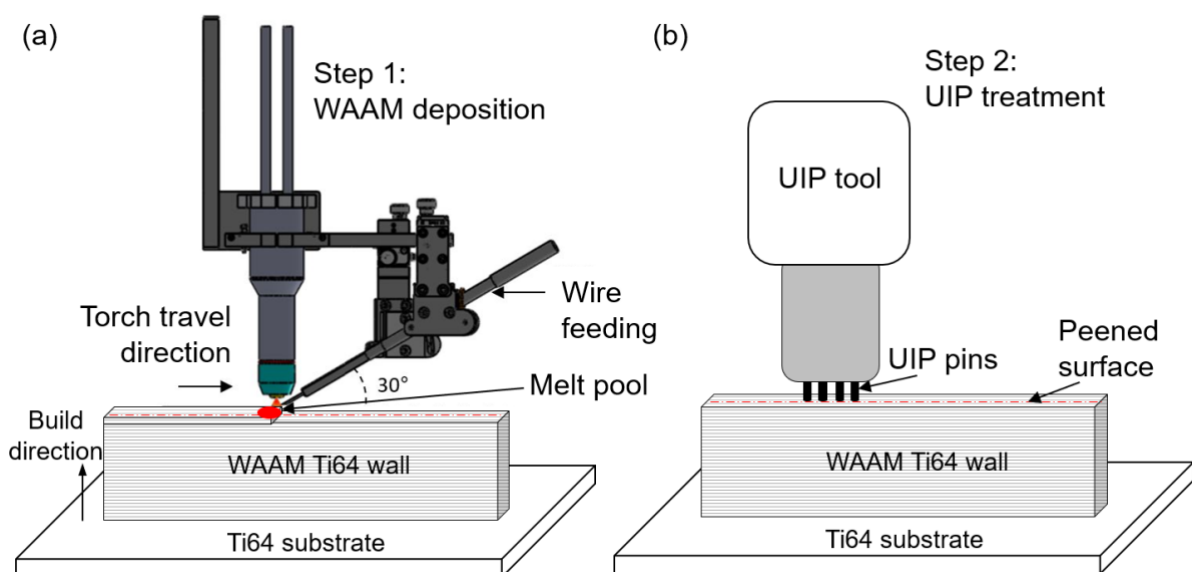
Fig. 1. Schematic of experimental set-up (a) WAAM Ti64 deposition overview, (b) inter-pass ultrasonic impact peening (UIP) head, with a single track WAAM Ti64 wall.

2. Materials and Methods

Two single track wide wall samples were deposited using the WAAM setup shown in Fig. 1, with 1.2 mm diameter Ti64 wire with the chemical compositions given in Table 1. The deposition process utilized an EWM^{TM} plasma energy source, and the specific process conditions are summarised in Table 2. Following the deposition of each layer, the top surface was allowed to cool to 40 ± 5 °C before UIP was performed with a Europe Technologies make UIP system. UIP treatment was conducted with a 520 ± 40 Hz impact frequency and utilized 4 in-line needles in the peening head, each having a diameter of 4 mm, which created indents of 1.8 ± 0.5 mm diameter along the wall's top surface. Variation in the indent sizes was primarily caused by the curved topology of the WAAM Ti64 wall. The impact energy imparted into the surface by each pin was estimated to be ~40 mJ and at the applied tool travel speed of 10 mm s^{-1} this resulted in a line energy of 5.9 J mm^{-1} to 13.5 J mm^{-1}. It should also be mentioned that these values are estimated using a conservative approach and the true line energy could be higher.

A first sample was built to a height of 100 mm with 84 layers; with peening applied to each layer using a single straight-track traversed approximately along the walls centre line, as depicted in Fig. 1. A second "stop-action" sample was also produced to allow deeper investigation into the mechanism of β-grain refinement. This was manufactured by initially building a wall to a height of 20 mm with 16 layers without inter-pass UIP, to establish a steady state coarse-columnar β-grain structure. Thereafter, the top layer was treated with UIP, using the same parameters as sample 1 (see Table 2), before an additional final layer was deposited. For this last layer, deposition was stopped midway along the wall by turning off the power supply, to freeze the melt pool and reveal the interaction between the energy source and the previously peened layer. Both samples were deposited on a hot-rolled wrought Ti64 substrate.

The reference frame employed throughout is; build, or layer normal direction, ND, energy source travel, or wall direction, WD, and wall transverse direction, TD. The samples were sectioned in the ND-TD and ND-WD planes for microstructural characterization. Metallographic preparation involved the standard procedure of grinding down to a 4000 grit finish, with SiC papers, followed by final polishing with 0.04 μm OPS for 15 minutes. After etching the final polished samples in Kroll's reagent for 3 minutes, large area optical images were captured using a Zeiss Axio Imager 2, equipped with an image stitching capability. Large area EBSD scanning was carried out using a field emission scanning electron microscope (FESEM) Thermo Scientific Apreo, integrated with Aztec software and a high speed Oxford Symmetry^R S3 EBSD detector at a 50 nA current and 20 kV voltage, with different step sizes depending

on the resolution required. Crystallographic related analyses were performed using Aztec Crystal 3.1 software. β-grain reconstruction was conducted using software developed by Davies and Wynne [46][47]. All EBSD maps are depicted with inverse pole figure (IPF)//ND colouration, with subgrain boundaries ($\geq 5°$) and grain boundaries ($\geq 10°$) delineated by white and black lines respectively. The texture data are represented in standard {001} pole figures for the β phase with units of multiples of random density (MRD) value. The β grain size was measured based on the equivalent circular diameter derived from identifying the grain areas ($\geq 10°$) in the Aztec Crystal software.

Table 1: Composition (in wt. %) of the Ti64 wire and substrate used in this work to produce the WAAM builds.

	Al	V	Fe	O	N	C	Si	Cu	Pd	Y	B	Ru	Bal
wire	6.15	3.9	0.18	0.15	0.008	0.022	0.014	0.008	0.002	0.002	0.002	0.003	Ti
substrate	6.41	4.1	0.16	0.18	0.004	0.021				0.001			Ti

Table 2: Process parameters used during WAAM plasma-arc deposition and UIP treatment of the single pass wide wall deposits.

	Wire feed speed (m/min)	Plasma torch travel speed (mm/s)	Current (A)	Peening tool travel speed (mm/s)
WAAM	2.1	3.7	180	
UIP				10

Estimates of the depth and intensity of subsurface local plastic strain caused by peening were made from higher resolution (2 μm step size) EBSD maps by using the Local Averaged Misorientation (EBSD-LAM) method, described in [35,38]. The LAM data was measured using average misorientations between points within a 11×11 square kernel from the centre point in that kernel. The EBSD-LAM method empirically correlates the LAM measurements within single α variant lamellar clusters to that measured in a systematic set of calibration samples with the same starting WAAM α lamellar microstructure, deformed cold in plane strain compression. It should be noted that the LAM calibration data was obtained at conventional (i.e. 10^{-3}) strain rates and this method is only able to quantify the plastic strain in a limited range of 4 – 12%, as no change can be observed for higher levels of plastic deformation and it is incapable of separating the effects of deformation from noise when the plastic strain is less than 4% [35].

The remelt depth refers to the average distance from the surface of the second-to-last layer deposited to the maximum depth of the fusion boundary resulting from the deposition of the final layer. Previously, in Ti64 WAAM deposits, the fusion boundary has been identified from a weak contrast white line revealed by etching using Kroll's regent and its local chemical activity has been attributed to transient micro-segregation of Fe, and slight changes in Al and V elements to the fusion boundary [16,38]. Thus, experimental identification of the fusion boundary relies entirely on the extant of segregation. This can prove challenging to identify, particularly in builds with lower Fe levels and could only be located in the current work intermittently upon close examination at high magnification. Therefore, in addition, Computational fluid Dynamics (CFD) simulations were used to predict the expected depth of the melt pool. This work was performed by using a previously developed and calibrated CFD model developed by Chen et al. [48–50]. Full details of this model and its dependence on the processing conditions can be found in refs. [48–52]. CFD simulations were preformed based on the current processing conditions (Table 2), and a resultant wall centreline (ND-WF) temperature distribution map is shown in Fig. 2, marked with the fusion boundary and locus of the β-transus peak temperature isotherm, which coincides with the position of the top of the last HAZ band. This model was performed for only one deposition layer on a pre-deposited 15 mm wall hight. The remelt depth was predicted to be 1.2 mm which was consistent with the experimental measurements.
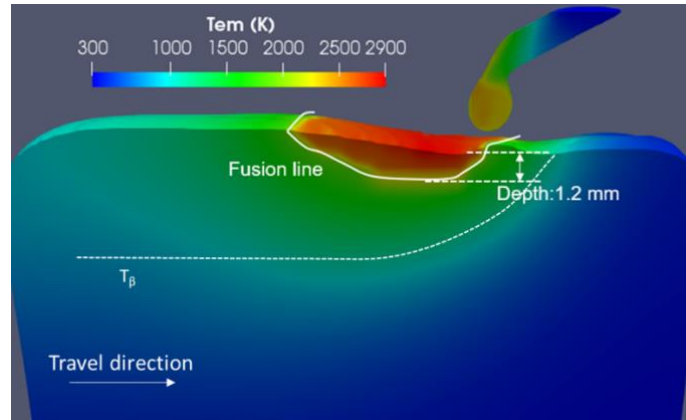

Fig. 2. CFD simulation showing the predicted temperature distribution for the ND-WD wall centre plane, depicting the fusion boundary, remelt depth, and locus of the β-transus peak temperature isotherm, which coincides with the position of top of the last HAZ band, using the experimental deposition conditions with the model developed by Chen et al. [44-48].

3.0 Results and Discussion

3.1 β grain refinement using UIP

Large area EBSD maps (Fig. 3b), taken from ND-TD cross sections through single-track wide walls built with UIP applied to every layer, are compared to that from a standard unrefined build in Fig. 3a taken from reference [24], showing the reconstructed β-phase grain orientations. From these maps it is apparent that the application of UIP to the top of every layer has resulted in substantial grain refinement of the β grains, although this was not as effective as for higher strain inter-pass deformation processes such as rolling [20,34]. The degree of refinement is also not very uniform across the wall's cross section, being concentrated in the centre with regions of coarse grains developing towards the wall's surfaces. This is to be expected, since UIP was only performed in a narrow 1.8 ± 0.5 mm width of contact along the approximate centreline of each layer in the current experiment. Just below the top surface a thin subsurface region can be seen, where poor reconstruction occurred due to the local surface deformation caused by the peening process (unindexed pixels highlighted in the dashed box in Fig. 3b). This poorly reconstructed region has a width consistent with the width of the peeing tool and is slightly off centre, which is reflected in the less grain refined surface regions being wider and having larger more <001>//ND oriented grains (red in the IPF map) on the left side of the deposit. The average grain diameter measured (based on equivalent circular diameter) from the refined middle portion of the microstructure, which underwent refinement due to the surface application of the UIP technique, was ~1.2 mm, compared to columnar grain lengths of ~ 1 - 2 cm's in the baseline sample.

Comparison of the texture strength in the <001> poles intensity in the {001} pole figure gives a value of 6.15 MRD along the build direction (Fig. 3d) from the whole map, which contains a strong near ND <001> pole due to the inclusion of the unrefined red near-surface columnar grains on the left-hand side of the wall. However, if the analysed area is restricted to the UIP-refined central region, the texture strength is significantly reduced to 5.8 MRD, which compares favourably with that achieved by pneumatic machine hammer peening (MHP) [38]. This is also far lower than that typically seen in an un-peened wall, which is in the range of 18-25 MRD (Fig. 3c, [37–40]) but still falls short of the β refinement achieved through inter-pass rolling, which can achieve a ~100 µm grain size and exhibit very weak textures with MRD values < 3.0 [20,34].
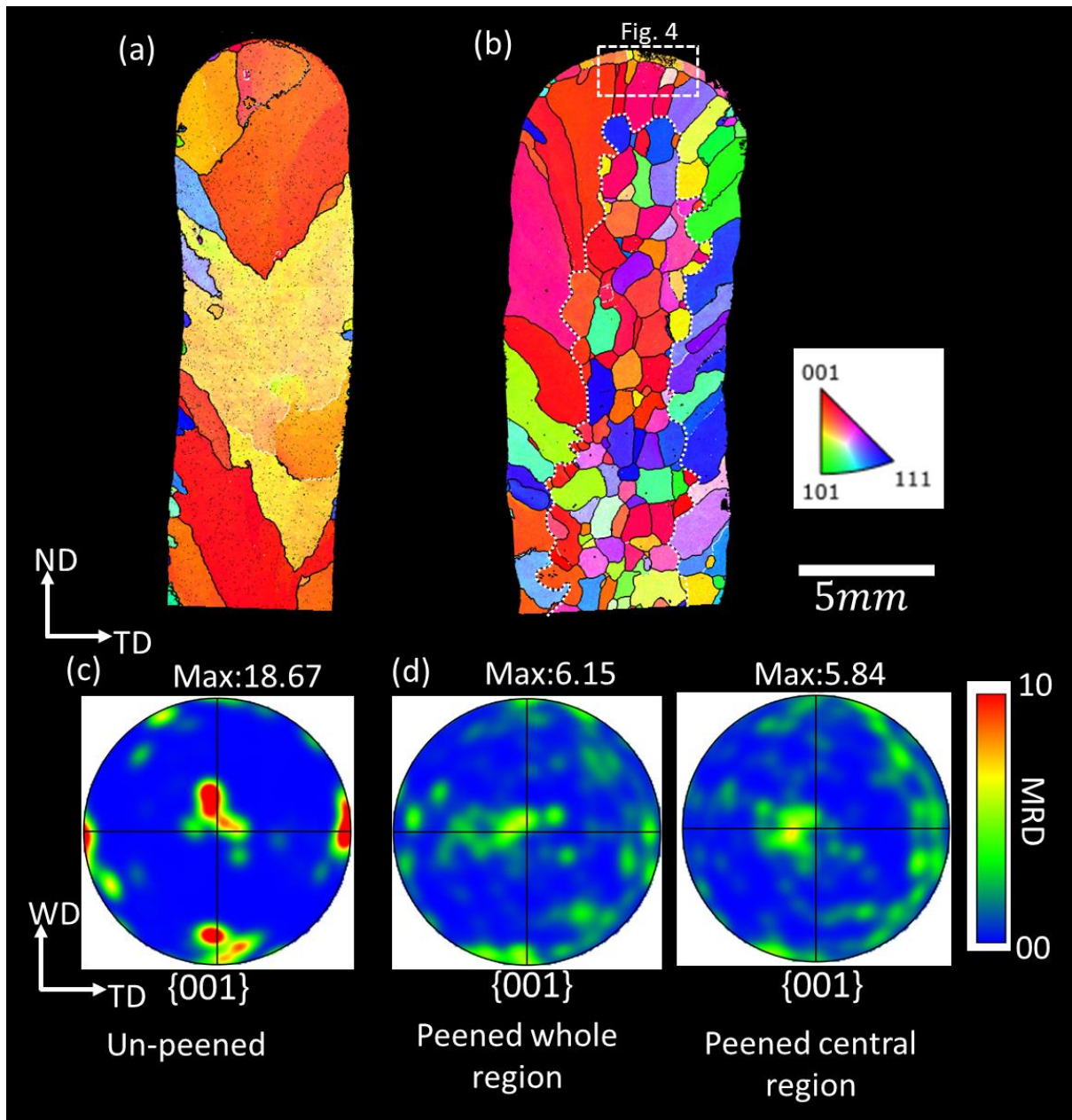
Fig. 3. ND-TD cross section EBSD maps comparing the reconstructed β phase grain structures seen in (a) a standard unrefined build [24] with that of (b) the sample that was UIP every layer. Comparative un-peened and peened {001} pole figures, depicting the textures obtained from each map are included in (c) and (d), respectively, with the texture of the central refined region affected by UIP, as indicated by the white dashed area, also provided for the UIP sample in (d). The white dashed box from the last layer in (b) highlights the thin region with a low level of successful indexing and reconstruction seen below the peened area, which is re-mapped at higher resolution in Fig. 4.
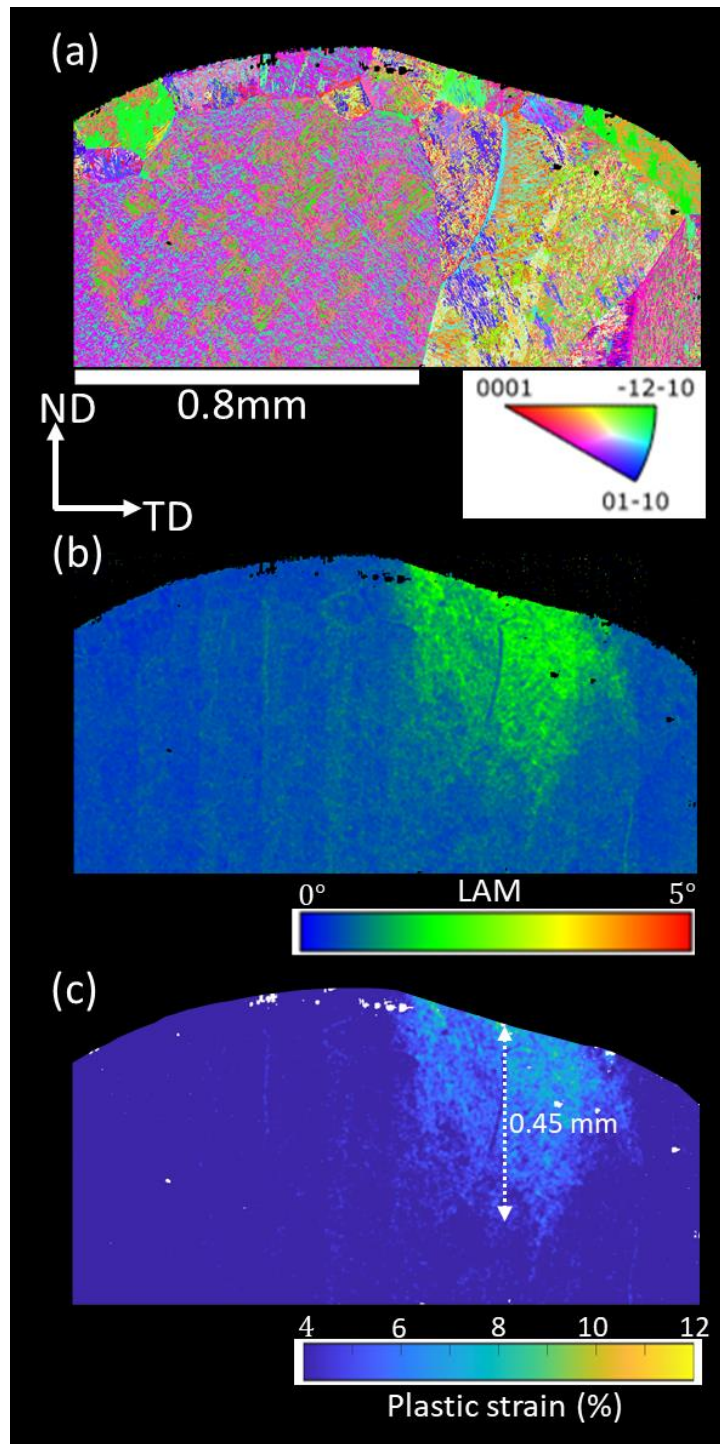
Fig. 4. High resolution EBSD analysis performed on a subsurface ND-TD section through the last deposited layer, showing evidence of deformation where UIP was performed (location indicated in Fig. 2b); (a) EBSD α-IPF map//ND, (b) local average misorientation (LAM) map and (c) with the local plastic strain distribution estimated by calibration using the EBSD-LAM method [35].

Fig. 4 highlights the subsurface local plastic strain distribution resulting from applying ultrasonic impact peening on the surface of the last deposited layer, as interpreted from a high-resolution EBSD α-IPF and LAM maps, performed across the poorly reconstructed region indicated in Fig. 3b. It should be

noted that EBSD-LAM method corelates the plastic strain to that generated by deformation at room temperature at conventional (i.e. 10^{-3}) strain rates and is only able to quantify the plastic strain in a restricted range of 4-12 %. It is therefore not certain how well this method applies to the high strain-rate deformation produced by UIP treatment. Nevertheless, Fig. 4 indicates that the subsurface impact from plastic deformation generated by ultrasonic peening was only sufficient to be detectable by both EBSD techniques in a thin region localized to the top surface. Evidence of a strain gradient is also evident below the surface to a depth of ~0.45 mm with the strain at the top surface determined by the EBSD-LAM method being of the order of 9 %. Fig. 3c thus indicates the plastic strain induced by peening was in the range of ~7 – 9 % and penetrated to a detectable level to a depth of 0.45 mm from the surface, which is similar to that seen for MHP in our previous study that employed a similar impact energy [37]. In comparison, the remelt depth in the WAAM samples was deeper than the detectable deformation depth, at ~ 1.2mm.

3.2 Stop-action sample

To better understand the grain refinement mechanism, the same 'stop-action' method previously employed with pneumatic machine hammer peening was deployed to study a UIP processed sample [38]. An initial deposit was first built with 15 layers added without peening to facilitate the formation of coarse-columnar β grains. UIP was then applied across the top surface of the last layer. A final layer was then deposited with the process stopped mid-way across the wall by rapidly extinguishing the arc to freeze the microstructure, as shown in Fig. 5. The WAAM deposition and UIP parameters are given in table 2. The optical image in Fig. 5a and EBSD map of the β grain orientations in Fig. 5b clearly show the original coarse columnar grain structure resulting from conventional WAAM deposition without UIP below the refined top layer. These grains have a strong <001>//ND fibre texture (red – in the IPF map) and are slightly tilted towards the energy source travel direction, WD, due to the shallow slope of the rear of the melt pool when they developed and grew normal to the solidification front. As would be expected from the profile of the thermal field generated by the energy source, the last HAZ band, which reflects the locus of where the peak temperature rise generated when the final track was added approaches the β-transus temperature, can be seen to be horizontal behind the now solidified melt pool and curve upwards ahead of the stop position. The position of the fusion boundary has also been identified from the weak etching contrast associated with Fe micro segregation (see ref. [16]) and has been outlined on the map to aid the reader, as it is difficult to see without closer inspection. It can be noted that the position of the HAZ band is very similar to that predicted in the CFD simulation in Fig. 2.

Two layered regions where β recrystallization and refinement has occurred are identified at the top of the wall trailing behind the melt pool in Fig. 4b (i.e. to the left side). A layer of finer grains can be seen that has grown downwards into the wall below the fusion boundary. Directional growth downward has caused these grains to develop a columnar aspect ratio, however this has occurred in the solid state. There is then a transition in the grain structure trailing the melt pool at the fusion boundary, from above which refined columnar grains have grown into the melt pool as solidification has occurred, to be left behind as the melt pool advanced. In Fig. 5b a small finer grain region can be seen immediately ahead of the stop position (right side in Fig. 5b) along with a subsurface layer further ahead of the energy source, where the coarse columnar grains from the previous layers are still evident, but there was poor reconstruction due to the deformation induced by the peening process. This interesting region is highlighted at higher magnification in Fig. 5c.

The contour of the recrystallised region seen in Fig. 5 follows the expected energy source thermal field profile (see Fig. 2), which generated a temperature gradient that falls off with distance ahead of, and below, the energy source. Similar to in the MHP process previously reported, it can be seen that recrystallization, involving the formation of new grain orientations, has only initiated to a limited depth within the peened region, which is less than the remelt depth. As such, these grains would be remelted by the next added layer. However, recrystallization initiates ahead of the melt pool where the temperature rise generated by the approaching energy source exceeded the transus temperature. The new grains that first formed in this region as α fully transforms to β, are extremely small, being of the order of 22 - 50 μm in size. These new grain orientations have only developed within the most heavily deformed region of the peened layer to a depth of ~ 0.5 mm. The small recrystallized grains can also be seen to reduce in size as the depth increases due to the subsurface gradient in prior deformation induced by peening. In addition, the new grains that formed where there was still just sufficient strain at the periphery of the recrystallized region to form new β orientations, continue to grow downwards, directionally, with their boundary migration following the direction of energy flow, which slants them forward normal to the curved temperature isotherm generated by the energy source, i.e. below a depth of 0.5 mm although there is not sufficient lattice strain to initiate new grain orientations grain boundary migration is still possible, of grains nucleated higher up in the deformation field, due to the deeper-lower stored energy introduced by peening. Nevertheless, grain growth downwards is restricted kinetically, in terms of grain-boundary mobility, by the falling temperature and the diminishing driving force as the stored energy in the reverted β phase, inherited from the originally deformed α-β lamellar microstructure, reduces with depth. This recrystallization process and subsequent directional grain growth thus created the lower band of refined grains seen in the partially

re-melted previously deposited layer that survive below the fusion boundary as the melt pool advanced.

As the translated energy source and melt pool moves forward, the fine recrystallized grains are remelted, and the larger partially melted forward-tilted columnar grains, formed by directional grain growth during recrystallization, become the new fusion boundary. These grains then act as seeds for epitaxial growth into the melt pool at its trailing edge. No new nucleation occurs during solidification so that a new columnar grain structure again develops in the melt pool from the recrystallized grains at the fusion boundary. However, this grain structure is greatly refined and has a weaker texture, relative to the coarse columnar grains that evolve after many deposition passes without the application of peening in the conventional WAAM process. In addition, as in the ND-WD plane the rear melt pool surface is tilted forwards towards the energy source travel direction and outwards towards the wall surfaces in the ND-TD plane, during solidification the preferred grain growth direction changes, relative to that of the recrystallized grains below the fusion boundary. In this context it is notable that to the left of the EBSD map in Fig. 5b the fine columnar grains seen in the fusion zone region, are consequently starting to tilt again forward towards WD in the opposite sense to the recrystallized grains, and growth selection is also occurring so that they are starting to develop the typical <100> solidification texture seen lower down in the wall (i.e. more 'red' grain orientations are present).

Overall, these observations thus show that when combined with the rapid high temperature thermal cycle generated by the energy source, inter-pass surface peening can be surprisingly effective in refining the coarse columnar grain structure normally seen in the WAAM process with titanium alloys, despite the shallow depth and relatively low level of plastic strain generated below each layer in the deposited material. When UIP is applied to every added layer, this refinement process also occurs in every layer and prevents a coarse columnar grain structure evolving and is therefore more effective than seen in a 'stop-action' experiment, when only the last layer is peened.

Finally, the above behaviour is remarkably consistent with our observations previously presented on the application of pneumatic machine hammer peening to WAAM inter-pass deformation [37]. This is despite the different nature of the UIP tool interaction with the material in terms of the lower impact energy and simultaneous impacts by multiple pins, rather than using a single hemi-spherical hammer tool with two orders higher impact energy. Despite the low impact energy of few milijoules, UIP provided repeated impacts with 4 pins impacting in-line, which resulted in a comparable value of line energy and exhibited a similar depth and level of grain refinement to pneumatic MHP processed Ti64. This implies that despite the differences in the UIP tool, and much of the energy being absorbed within

the depth of deposited layer, the deformation induced by the lower energy individual impacts does not appear to significantly change the recrystallization process.
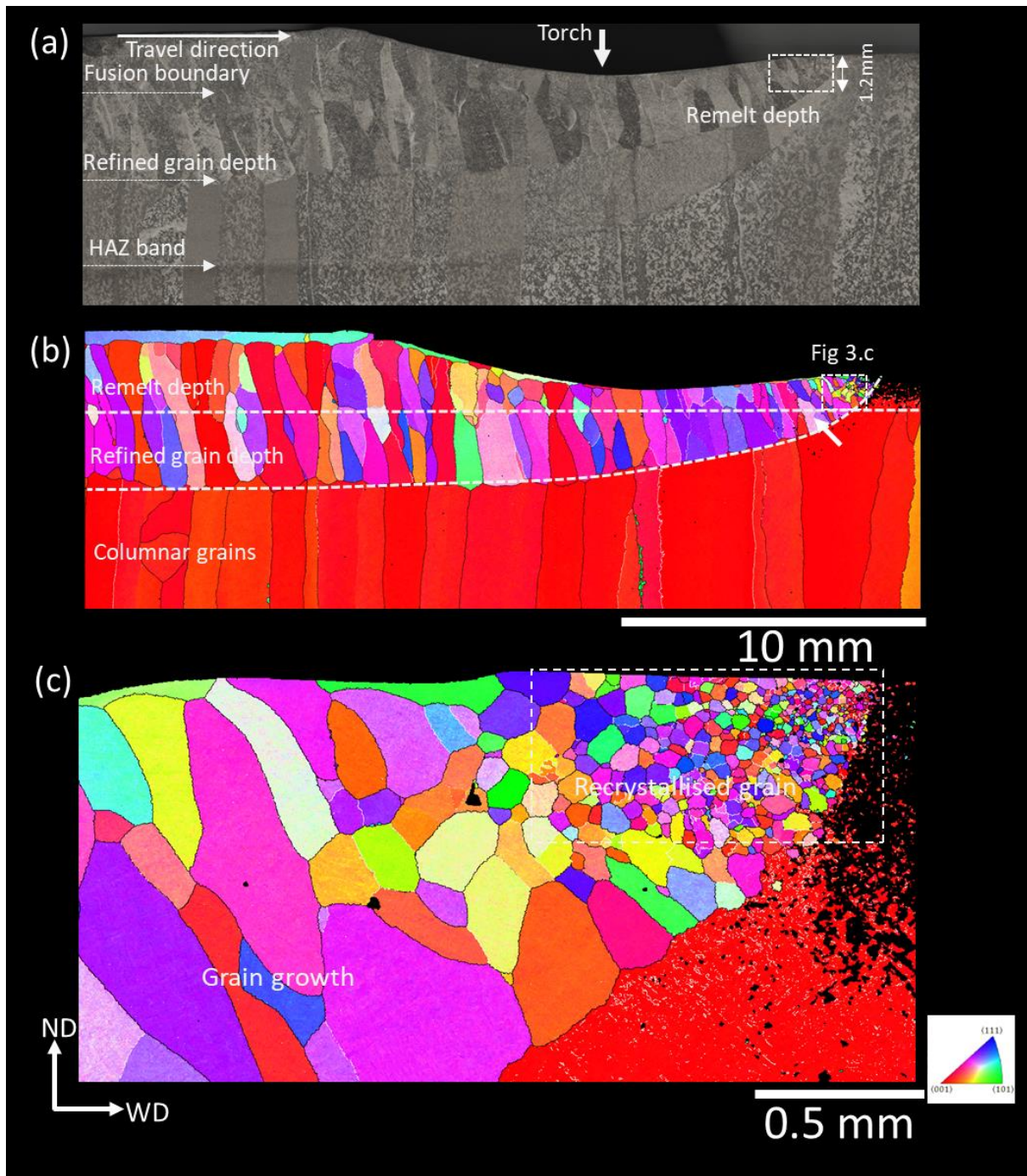

Fig. 5. Optical image and EBSD maps taken from a wall centreline WD-ND sections of the stop action test sample, showing (a) an optical macro view of the stop position, with the fusion boundary and last HAZ band profiles identified, (b) the same area following EBSD mapping and reconstruction of the β grain structure, and (c) a higher resolution map of the small region (marked top right in (b)) where recrystallization recyclization first occurs *ahead of* the melt pool. The dark pixels to the right at the top

of (c) where reconstruction was not possible are indicative of the depth and extent of deformation induced by the peening tool.

4.0 Conclusions

By combining advanced EBSD characterization with a 'stop action' technique, inter-pass deformation by ultrasonic impact peening has been shown to be effective in refining the coarse columnar, strongly textured, β-grain structure normally seen in wire-arc AM deposits, produced with Ti64. Ultrasonic impact peening resulted in both significant β grain refinement and texture weakening, despite the remelt depth being greater than the depth of β recrystallization induced by UIP.

Relatively low levels of subsurface plastic deformation, generated by UIP, of the order of 6-7%, to a shallow depth of only ~0.45 mm was sufficient to produce grain refinement. Stop-action experiments showed this could occur because new β-grain orientations formed in this thin-deformed subsurface layer by recrystallization in re-heating above the β-transus, as the temperature rapidly increased ahead of the melt pool when the energy source was translated. These recrystallized grains then grew downwards into the deposit to a greater depth and were able to survive remelting to act as nucleation sites at the fusion boundary for epitaxial regrowth during subsequent solidification at the melt pool rear.

The overall results were consistent with previous observations on the application of pneumatic machine hammer peening to WAAM inter-pass deformation. Although UIP uses a lower peak force and two orders of lower impact energy, the much higher number of impacts per unit length achieved by the action of the high frequency multiple pins resulted in a similar line energy as a single pinned high energy impact pneumatic machine hammer tool. This study thus confirms that recrystallisation behaviour is controlled by the amount of line energy applied during the peening step, irrespective of the differences in tool specifications.

Acknowledgement

References:

[1]   D.L. Bourell, Perspectives on Additive Manufacturing, Annu. Rev. Mater. Res. 46 (2016) 1–18. https://doi.org/10.1146/annurev-matsci-070115-031606.

[2]   T. DebRoy, H.L. Wei, J.S. Zuback, T. Mukherjee, J.W. Elmer, J.O. Milewski, A.M. Beese, A. Wilson-Heid, A. De, W. Zhang, Additive manufacturing of metallic components – Process, structure and properties, Progress in Materials Science 92 (2018) 112–224. https://doi.org/10.1016/j.pmatsci.2017.10.001.

[3]   D. Ding, Z. Pan, D. Cuiuri, H. Li, Wire-feed additive manufacturing of metal components: technologies, developments and future interests, Int J Adv Manuf Technol 81 (2015) 465–481. https://doi.org/10.1007/s00170-015-7077-3.

[4]   W.E. Frazier, Metal Additive Manufacturing: A Review, J. of Materi Eng and Perform 23 (2014) 1917–1928. https://doi.org/10.1007/s11665-014-0958-z.

[5]   S.W. Williams, F. Martina, A.C. Addison, J. Ding, G. Pardal, P. Colegrove, Wire + Arc Additive Manufacturing, Materials Science and Technology 32 (2016) 641–647. https://doi.org/10.1179/1743284715Y.0000000073.

[6]   S.M. Kelly, S.L. Kampe, Microstructural evolution in laser-deposited multilayer Ti-6Al-4V builds: Part I. Microstructural characterization, Metall Mater Trans A 35 (2004) 1861–1867. https://doi.org/10.1007/s11661-004-0094-8.

[7]   F. Wang, S. Williams, M. Rush, Morphology investigation on direct current pulsed gas tungsten arc welded additive layer manufactured Ti6Al4V alloy, Int J Adv Manuf Technol 57 (2011) 597–603. https://doi.org/10.1007/s00170-011-3299-1.

[8]   E. Brandl, A. Schoberth, C. Leyens, Morphology, microstructure, and hardness of titanium (Ti-6Al-4V) blocks deposited by wire-feed additive layer manufacturing (ALM), Materials Science and Engineering: A 532 (2012) 295–307. https://doi.org/10.1016/j.msea.2011.10.095.

[9]   A.A. Antonysamy, P.B. Prangnell, J. Meyer, Effect of Wall Thickness Transitions on Texture and Grain Structure in Additive Layer Manufacture (ALM) of Ti-6Al-4V, MSF 706–709 (2012) 205–210. https://doi.org/10.4028/www.scientific.net/MSF.706-709.205.

[10]   S.S. Al-Bermani, M.L. Blackmore, W. Zhang, I. Todd, The Origin of Microstructural Diversity, Texture, and Mechanical Properties in Electron Beam Melted Ti-6Al-4V, Metall Mater Trans A 41 (2010) 3422–3434. https://doi.org/10.1007/s11661-010-0397-x.

[11]   P.A. Kobryn, S.L. Semiatin, Microstructure and texture evolution during solidification processing of Ti–6Al–4V, Journal of Materials Processing Technology 135 (2003) 330–339. https://doi.org/10.1016/S0924-0136(02)00865-8.

[12]   M.J. Bermingham, S.D. McDonald, M.S. Dargusch, D.H. StJohn, Grain-refinement mechanisms in titanium alloys, J. Mater. Res. 23 (2008) 97–104. https://doi.org/10.1557/JMR.2008.0002.

[13]   A.A. Antonysamy, J. Meyer, P.B. Prangnell, Effect of build geometry on the β-grain structure and texture in additive manufacture of Ti6Al4V by selective electron beam melting, Materials Characterization 84 (2013) 153–168. https://doi.org/10.1016/j.matchar.2013.07.012.

[14]   M.J. Bermingham, S.D. McDonald, D.H. StJohn, M.S. Dargusch, Segregation and grain refinement in cast titanium alloys, J. Mater. Res. 24 (2009) 1529–1535. https://doi.org/10.1557/jmr.2009.0173.

[15]   P.A. Kobryn, S.L. Semiatin, Microstructure and texture evolution during solidification processing of Ti–6Al–4V, Journal of Materials Processing Technology 135 (2003) 330–339. https://doi.org/10.1016/S0924-0136(02)00865-8.

[16]   A. Ho, H. Zhao, J.W. Fellowes, F. Martina, A.E. Davis, P.B. Prangnell, On the origin of microstructural banding in Ti-6Al4V wire-arc based high deposition rate additive manufacturing, Acta Materialia 166 (2019) 306–323. https://doi.org/10.1016/j.actamat.2018.12.038.

[17]   A.E. Davis, X. Zeng, R. Thomas, J.R. Kennedy, J. Donoghue, A. Gholinia, P.B. Prangnell, J.Q. Da Fonseca, Optimising large-area crystal orientation mapping of nanoscale β phase in α + β

titanium alloys using EBSD, Materials Characterization 194 (2022) 112371. https://doi.org/10.1016/j.matchar.2022.112371.

[18] G.C. Obasi, S. Birosca, J. Quinta Da Fonseca, M. Preuss, Effect of β grain growth on variant selection and texture memory effect during α→β→α phase transformation in Ti–6 Al–4 V, Acta Materialia 60 (2012) 1048–1058. https://doi.org/10.1016/j.actamat.2011.10.038.

[19] F. Wang, S. Williams, P. Colegrove, A.A. Antonysamy, Microstructure and Mechanical Properties of Wire and Arc Additive Manufactured Ti-6Al-4V, Metall Mater Trans A 44 (2013) 968–977. https://doi.org/10.1007/s11661-012-1444-6.

[20] J. Donoghue, A.A. Antonysamy, F. Martina, P.A. Colegrove, S.W. Williams, P.B. Prangnell, The effectiveness of combining rolling deformation with Wire–Arc Additive Manufacture on β-grain refinement and texture modification in Ti–6Al–4V, Materials Characterization 114 (2016) 103–114. https://doi.org/10.1016/j.matchar.2016.02.001.

[21] D. Lunt, A. Ho, A. Davis, A. Harte, F. Martina, J. Quinta Da Fonseca, P. Prangnell, The effect of loading direction on strain localisation in wire arc additively manufactured Ti–6Al–4V, Materials Science and Engineering: A 788 (2020) 139608. https://doi.org/10.1016/j.msea.2020.139608.

[22] A.K. Syed, X. Zhang, A.E. Davis, J.R. Kennedy, F. Martina, J. Ding, S. Williams, P.B. Prangnell, Effect of deposition strategies on fatigue crack growth behaviour of wire + arc additive manufactured titanium alloy Ti–6Al–4V, Materials Science and Engineering: A 814 (2021) 141194. https://doi.org/10.1016/j.msea.2021.141194.

[23] G. Xian, J.M. Oh, J. Lee, S.M. Cho, J.-T. Yeom, Y. Choi, N. Kang, Effect of heat input on microstructure and mechanical property of wire-arc additive manufactured Ti-6Al-4V alloy, Weld World 66 (2022) 847–861. https://doi.org/10.1007/s40194-021-01248-3.

[24] A.E. Davis, J. Wainwright, V.K. Sahu, D. Dreelan, X. Chen, J. Ding, T. Flint, S. Williams, P.B. Prangnell, Achieving a Columnar-to-Equiaxed Transition Through Dendrite Twinning in High Deposition Rate Additively Manufactured Titanium Alloys, Metall Mater Trans A (2024). https://doi.org/10.1007/s11661-024-07388-7.

[25] J. Wang, X. Lin, J. Wang, H. Yang, Y. Zhou, C. Wang, Q. Li, W. Huang, Grain morphology evolution and texture characterization of wire and arc additive manufactured Ti-6Al-4V, Journal of Alloys and Compounds 768 (2018) 97–113. https://doi.org/10.1016/j.jallcom.2018.07.235.

[26] J. Wainwright, S. Williams, J. Ding, Refinement of Ti-6Al-4V prior-β grain structure in the as-deposited condition via process control during wire-direct energy deposition, Additive Manufacturing 74 (2023) 103712. https://doi.org/10.1016/j.addma.2023.103712.

[27] K. Zhang, X. Tian, M. Bermingham, J. Rao, Q. Jia, Y. Zhu, X. Wu, S. Cao, A. Huang, Effects of boron addition on microstructures and mechanical properties of Ti-6Al-4V manufactured by direct laser deposition, Materials & Design 184 (2019) 108191. https://doi.org/10.1016/j.matdes.2019.108191.

[28] J.R. Kennedy, A.E. Davis, A.E. Caballero, S. Williams, E.J. Pickering, P.B. Prangnell, The potential for grain refinement of Wire-Arc Additive Manufactured (WAAM) Ti-6Al-4V by ZrN and TiN inoculation, Additive Manufacturing 40 (2021) 101928. https://doi.org/10.1016/j.addma.2021.101928.

[29] J.R. Kennedy, A.E. Davis, A.E. Caballero, N. Byres, S. Williams, E.J. Pickering, P.B. Prangnell, β Grain refinement by yttrium addition in Ti-6Al-4V Wire-Arc Additive Manufacturing, Journal of Alloys and Compounds 895 (2022) 162735. https://doi.org/10.1016/j.jallcom.2021.162735.

[30] J.R. Kennedy, A.E. Davis, A.E. Caballero, E.J. Pickering, P.B. Prangnell, β grain refinement during solidification of Ti-6Al-4V in Wire-Arc Additive Manufacturing (WAAM), IOP Conf. Ser.: Mater. Sci. Eng. 1274 (2023) 012005. https://doi.org/10.1088/1757-899X/1274/1/012005.

[31] M.J. Bermingham, D.H. StJohn, J. Krynen, S. Tedman-Jones, M.S. Dargusch, Promoting the columnar to equiaxed transition and grain refinement of titanium alloys during additive manufacturing, Acta Materialia 168 (2019) 261–274. https://doi.org/10.1016/j.actamat.2019.02.020.

[32] J.R. Kennedy, A.E. Davis, A. Caballero, A. Garner, J. Donoghue, S. Williams, J. Zollinger, E. Bouzy, E.J. Pickering, P.B. Prangnell, Isomorphic grain inoculation in Ti-6Al-4V during additive manufacturing, Materials Letters: X 8 (2020) 100057. https://doi.org/10.1016/j.mlblux.2020.100057.

[33] K. Zhang, X. Tian, M. Bermingham, J. Rao, Q. Jia, Y. Zhu, X. Wu, S. Cao, A. Huang, Effects of boron addition on microstructures and mechanical properties of Ti-6Al-4V manufactured by direct laser deposition, Materials & Design 184 (2019) 108191. https://doi.org/10.1016/j.matdes.2019.108191.

[34] J. Donoghue, A.E. Davis, C.S. Daniel, A. Garner, F. Martina, J. Quinta Da Fonseca, P.B. Prangnell, On the observation of annealing twins during simulating β-grain refinement in Ti–6Al–4V high deposition rate AM with in-process deformation, Acta Materialia 186 (2020) 229–241. https://doi.org/10.1016/j.actamat.2020.01.009.

[35] A.E. Davis, J.R. Hönnige, F. Martina, P.B. Prangnell, Quantification of strain fields and grain refinement in Ti-6Al-4V inter-pass rolled wire-arc AM by EBSD misorientation analysis, Materials Characterization 170 (2020) 110673. https://doi.org/10.1016/j.matchar.2020.110673.

[36] A.E. Davis, A. Caballero, P.B. Prangnell, Confirmation of rapid-heating β recrystallization in wire-arc additively manufactured Ti-6Al-4V, Materialia 13 (2020) 100857. https://doi.org/10.1016/j.mtla.2020.100857.

[37] L. Neto, S. Williams, A.E. Davis, J.R. Kennedy, Effect of Machine Hammer Peening Conditions on β Grain Refinement of Additively Manufactured Ti-6Al-4V, Metals 13 (2023) 1888. https://doi.org/10.3390/met13111888.

[38] J.R. Hönnige, A.E. Davis, A. Ho, J.R. Kennedy, L. Neto, P. Prangnell, S. Williams, The Effectiveness of Grain Refinement by Machine Hammer Peening in High Deposition Rate Wire-Arc AM Ti-6Al-4V, Metall Mater Trans A 51 (2020) 3692–3703. https://doi.org/10.1007/s11661-020-05781-6.

[39] M. Zhang, C. Liu, X. Shi, X. Chen, C. Chen, J. Zuo, J. Lu, S. Ma, Residual Stress, Defects and Grain Morphology of Ti-6Al-4V Alloy Produced by Ultrasonic Impact Treatment Assisted Selective Laser Melting, Applied Sciences 6 (2016) 304. https://doi.org/10.3390/app6110304.

[40] A.I. Gorunov, Additive manufacturing of Ti6Al4V parts using ultrasonic assisted direct energy deposition, Journal of Manufacturing Processes 59 (2020) 545–556. https://doi.org/10.1016/j.jmapro.2020.10.024.

[41] J.H. Luan, Z.B. Jiao, G. Chen, C.T. Liu, Effects of boron additions and solutionizing treatments on microstructures and ductility of forged Ti–6Al–4V alloys, Journal of Alloys and Compounds 624 (2015) 170–178. https://doi.org/10.1016/j.jallcom.2014.11.008.

[42] J.R. Hönnige, P. Colegrove, S. Williams, Improvement of microstructure and mechanical properties in Wire + Arc Additively Manufactured Ti-6Al-4V with Machine Hammer Peening, Procedia Engineering 216 (2017) 8–17. https://doi.org/10.1016/j.proeng.2018.02.083.

[43] L. Lan, H. Niu, Y. Cui, X. Chen, Local shape adjustment and residual stresses of integrally stiffened panel induced by mechanical hammer peening, Journal of Manufacturing Processes 91 (2023) 99–109. https://doi.org/10.1016/j.jmapro.2023.02.044.

[44] Lechner C, Bleicher F, Habersohn C, Bauer C and Goessinger S, The Use of Machine Hammer Peening Technology for Smoothening And Structuring of Surfaces, 23rd International DAAAM Symposium, Austria (2012).

[45] J. Gou, Z. Wang, S. Hu, J. Shen, Y. Tian, G. Zhao, Y. Chen, Effects of ultrasonic peening treatment in three directions on grain refinement and anisotropy of cold metal transfer additive manufactured Ti-6Al-4V thin wall structure, Journal of Manufacturing Processes 54 (2020) 148–157. https://doi.org/10.1016/j.jmapro.2020.03.010.

[46] P.S. Davies, B.P. Wynne, W.M. Rainforth, M.J. Thomas, P.L. Threadgill, Development of Microstructure and Crystallographic Texture during Stationary Shoulder Friction Stir Welding of Ti-6Al-4V, Metall Mater Trans A 42 (2011) 2278–2289. https://doi.org/10.1007/s11661-011-0606-2.

[47] P.S. Davies, An investigation of microstructure and texture evolution in the Near-α titanium alloy timetal 834, (2009).

[48] X. Chen, C. Wang, J. Ding, P. Bridgeman, S. Williams, A three-dimensional wire-feeding model for heat and metal transfer, fluid flow, and bead shape in wire plasma arc additive manufacturing, Journal of Manufacturing Processes 83 (2022) 300–312. https://doi.org/10.1016/j.jmapro.2022.09.012.

[49] X. Chen, C. Wang, J. Ding, R. Qu, Y. Wang, G. Pardal, S. Williams, Thermal fluid dynamics of the effect of filler wire on deposition rate and bead formation intending plasma arc-based DED, Journal of Manufacturing Processes 107 (2023) 199–209. https://doi.org/10.1016/j.jmapro.2023.10.020.

[50] V.R. Voller, A.D. Brent, C. Prakash, The modelling of heat, mass and solute transport in solidification systems, International Journal of Heat and Mass Transfer 32 (1989) 1719–1731. https://doi.org/10.1016/0017-9310(89)90054-9.

[51] R. Hu, X. Chen, G. Yang, S. Gong, S. Pang, Metal transfer in wire feeding-based electron beam 3D printing: Modes, dynamics, and transition criterion, International Journal of Heat and Mass Transfer 126 (2018) 877–887. https://doi.org/10.1016/j.ijheatmasstransfer.2018.06.033.

[52] C.W. Hirt, B.D. Nichols, Volume of fluid (VOF) method for the dynamics of free boundaries, Journal of Computational Physics 39 (1981) 201–225. https://doi.org/10.1016/0021-9991(81)90145-5.